COMMUNICATIONS IN SCIENCE AND TECHNOLOGY
Homepage: cst.kipmi.or.id

Cigarette filter butts-derived activated carbon with free binder electrode design for solid-state supercapacitor application

Yanuar Hamzah[a,*], Erman Taer[a], Apriwandi Apriwandi[a], Faridah Lisa Supian[b], Niloofar Mozaffari[c], Nastaran Mozaffari[d]

[a]*Department of Physics, Faculty of Mathematic and Natural Sciences, University of Riau, Pekanbaru 28293, Indonesia*
[b]*Department of Physics, Faculty of Science and Mathematics, Sultan Indris University of Education (UPSI), Perak 35900, Malaysia*
[c]*Department of Physics, Faculty of Sciences, Science and Research Branch, Islamic Azad University, Tehran 1477893855, Iran*
[d]*Department of Environmental Engineering, Faculty of Natural Resources and Environment, Science and Research Branch, Islamic Azad University, Tehran 147789385, Iran*

Article history:
Received: 15 August 2023 / Received in revised form: 14 November 2023 / Accepted: 28 November 2023

Abstract

The aim of this research is to formulate activated carbon monolith from hazardous waste of cigarette filter butts (CFB) for electrode material monolith design in solid-state supercapacitor application. Potassium hydroxide (KOH) was selected for activation. The ratio of CFB to KOH varied in terms of weight between 1:2 and 1:4, thereby obtaining activated cigarette filter carbon (ACFC). The carbon that has been obtained is designed to be solidly in the form of an additive-free monolith. Monolith-activated carbon is physically characterized to examine thermal decomposition profiles (pre-carbonized), structure, composition, morphology, surface area adsorption, and electrochemical measurements. The optimum precursor was marked with high wettability with self-O-doped of 5.44%.in carbon content of 94.56%. Activated carbon electrodes prepared from ACFCs showed an optimum specific capacitance of ~87.17 F g^{-1}, which is a more ecologically responsible method of producing supercapacitors.

Keywords: Cigarette filter; activated carbon monolith; activated cigarette filter carbon; KOH activation; supercapacitor

1. Introduction

Activated carbon is widely used as a functional material in a wide range of uses [1]. This material can be used as an absorbent due to its porous structure and high specific surface area [2]. Activated carbon can be made from a range of biomass materials, including cellulose fiber from cigarette filter butts (CFB) waste [3]. CFB is a toxic solid waste that pollutes the atmosphere. Cellulose acetate makes up the largest percentage of CFBs, in which each filter contains 1200 cellulose acetate fibers with a Y-shaped cross-section [4,5]. According to a Euro-monitor International survey, approximately 5.7 trillion cigarette filters are wasted annually, with a 25% increase predicted by 2025 [6]. Unfortunately, large amounts of CFBs are unutilized and released into the environment.

Recently, researchers revealed on the various uses for cigarette filters. As well known, CFB 95% of cigarette filters are made of cellulose acetate, this cellulose compound can be converted into carbon material via thermochemical or other chemical methods for varying application. For example, Liu and a coworker created an oil spill cleanup using recycled cigarette filters [7]. They investigated a method for water-oil separation using super-hydrophilic and super-hydrophobic cigarette filters. A group of researchers used sodium hydroxide (NaOH) solution to transform CFBs into a super-hydrophobic material [8]. Li et al. (2021) developed a cigarette filter-based to flexible pressure sensor [9]. Rahman et al. (2020) also used cigarette filter fibers as an asphalt concrete for high-resistance clay bricks [10]. For fluorescence detection, N and S-co-doped carbon quantum dots were produced from cigarette filters [11,12]. CFBs are also used in cellulose pulp, biofilm-activated sludge reactors, and alternative uranium removal sorbents [13–15]. As of present, we are aware of four reports on the preparation of active carbon using CFB waste as energy storage. N-doped waste cigarette butts with a carbon anode have been created for lithium-ion batteries (LIB) and sodium-ion batteries (SIB) [16,17]. Several studies was produce N-doped carbon by pyrolyzing a cigarette filter as a supercapacitor [18,19]. In general, biomass-based carbon materials are considered superior as supercapacitor devices due to their abundant availability and amazing carbon material characteristics [1,20]. However, their energy density is relatively variable and is considered to be low. one possible technique is to add doping in the material. On this side, CFBs are considered to potentially exhibit doping due to the contribution of their

* Corresponding author.
Email: yanuar.hamzah@lecturer.unri.ac.id
https://doi.org/10.21924/cst.8.2.2023.1252

various constituents such as NO_2, cellulose acetate etc [4,21].

Meanwhile, many researchers have created potassium hydroxide (KOH)-activated carbon fiber synthesis. Chemical activation with KOH is a well-known method for activating carbon compounds with large surface areas [22,23]. Their significant effects were fully illustrated in previous studies [24,25], which suggested that KOH can optimize pore formation and surface area in carbon materials. Activation is commonly accomplished by heating a combination of carbon, KOH, and mesoporous carbon under N_2 gas atmosphere at temperatures ranging from 400 °C to 1000 °C [26,27]. In general, the amount of KOH and the activation procedure of the pre-carbonized carbon might influence the structural information of mesoporous carbon by increasing surface area, optimizing pore size, designing a hierarchical pore structure, and regulating carbon morphology [28,29]. Due to its large surface area, active carbon works as an adsorbent material. Because of its abundance and conversion to activated carbon material, CFB waste was chosen as a hazardous waste material and a potential alternative, limiting its disposal in the environment.

The current study investigated the formation and characterization of active carbon monoliths from CFB waste using KOH activation. We carbonized as a way of making use of an electrode. This research aims to provide a recycling preparation of cigarette filter waste as an alternative to activated carbon monoliths in accordance with an increase in KOH activation. The most influential preliminary results in this research will be presented based on physical characterization data analysis and electrochemical measurement. Thermal decomposition, morphology, and elemental analysis of the activated ACFCs were observed by thermo-gravimetric analysis (TGA), scanning electrode microscope (SEM), and energy-dispersive x-ray spectroscopy (EDX). Crystallographic characteristics are also evaluated using x-ray diffraction (XRD) to comprehend structural changes. Nitrogen adsorption isotherms were measured to determine the surface area. Furthermore, cyclic voltammetry (CV) measurements were performed to investigate the specific capacitance.

2. Materials and Methods

2.1. Preparation of ACFC

For this aim, activated cigarette filter carbon (ACFC) pellets were prepared. CFB was obtained from a trash can in a smoking room in the Peknbaru area, Riau, Indonesia. Cigarette waste is cleaned and the cigarette butts are taken. To check out the effect of pre-contained activated carbon, only half of the filters were used in this study. Cigarette filters were cleaned with hot water, then immersed in 96% ethanol, rinsed with distilled water, and air dried. For 3 hours, the cigarette filters were dried in a vacuum oven at 230°C. The CFB was pre-carbonized for 3 hours at 250°C. Then it was ball milled for about 20 hours before being sieved to a particle size of 100 microns. The CFB powders were then used as precursors for 2 hours of chemical activation with KOH solution at 80°C. The CFB-to-KOH ratio varied between 1:2 and 1:4, and the resulting carbon was labeled as ACFC-1 and ACFC-2, respectively.

All the sample grains are prepared into a pellet with a mold size of 20 mm in diameter and 8 tons of compressive force. The samples were carbonized under N_2 atmosphere (1.5 L min^{-1}) at 600°C for 7 to 8 hours, respectively. To create an ACFC monolith, the heating rate was adjusted to 5°C/min. The ACFC electrodes were polished to 0.5 mm thickness and then washed with distilled water until the pH of the filtrating solutions was neutral (pH = 7.0) and washed with distilled water. ACFCs have a weight of 50 mg and a dimension of 15.5 mm x 0.5 mm. The cell was made up of two ACFC electrodes and two 0.05 mm thick stainless steel current collectors. The electrode components are then stacked between two 15.5 mm acrylic case sections and compactly assembled using an inward force of a clamp (represented as ACFC-1 and ACFC-2 cells).

2.2. Characterizations

The thermal decomposition of an ACFCs electrode was evaluated using a TGA Shimadzu TGA-50 at temperatures that ranged from 30 to 600°C with a heating rate of 1°C per minute in atmospheric liquid nitrogen. Structural properties were determined using an XRD Siemens D5000 with Cu Kα targets (Cu-Kα =1.5418Å) at a scan rate of 0.5°C min^{-1} and two intervals ranging from 10 to 100°C. In addition, The average crystalline size of ACFCs at 9.15 nm was calculated using the Scherer formula with d=0.9 ⁄ β cos θ, l is the wavelength 1.5418 Å, θ is the Bragg diffraction angle, and β is the FWHM, based on the full wave half maximum (FWHM) and the (101) reflection at 2θ~25.25° [30–32]. SEM and EDX were used to examine the morphology and composition (JEOL-JSM 6360LA). Furthermore, the particle size displayed by SEM is measured using IC Measure software. Adsorption-isotherms-desorption experiments were performed on a Quanta Chrome Instrument with liquid nitrogen flowing at 77 K. BET equation is introduced as [33,34].

$$\frac{1}{W\left[\frac{P}{P_0}-1\right]}=\frac{1}{W_mC}+\frac{C-1}{W_mC}\left(\frac{P}{P_0}\right) \tag{1}$$

Where the relative pressure has shown as P/P_0 We can determine the slope (s) and intercept (i) of the linear plot as in Eq. (2) and (3).

$$s=\frac{C-1}{W_mC} \tag{2}$$

$$i=\frac{1}{W_mC} \tag{3}$$

W_m is the mass of adsorbate that is forming a mono-layer. W_m is calculated by Eq. (4).

$$W_m=\frac{1}{s+i} \tag{4}$$

C is the BET constant used to demonstrate the durability of

the interaction between adsorbate and adsorbent, and it is calculated as in Eq. (5).

$$C = \frac{s}{i} + 1 \tag{5}$$

The high value of C is an indication of the high porosity of the sample, whose formation of several layers occurs faster. Therefore, the surface area is defined as in Eq. (6)

$$S = \frac{W_m N \sigma}{M} \tag{6}$$

In the above equation, N, σ, and M represent Avogadro's number, gas cross-sectional area, and adsorbate molecular weight, respectively.

The fraction of surface is obtained as in Eq. (7).

$$(\theta_0)_m = \frac{\sqrt{C} - 1}{C - 1} \tag{7}$$

The Lowell equation is introduced [35].

$$(\theta_i)_m = C\left(\frac{\sqrt{C} - 1}{C - 1}\right)^{i+1} \tag{8}$$

Where θ_i is the fraction surface coverage of molecules layers in the depth of i.

The CV measurements were carried out at room temperature using a two-electrode setup in a 6 M aqueous KOH solution (Rad-Er 5841). The CV was measured at a scan rate of 1 mV s^{-1} in the potential range of 0 to 1 V.

3. Results and Discussion

Figure 1 depicts the TG and DTG profiles of pre-carbonized CFB. CFB samples lost around 74.3% of their total weight at temperatures ranging from 250 to 400°C. In more detail, cellulose compounds decompose significantly at temperatures of 250-400°C [36], followed by liginin compounds from 350-700°C [37,38]. The DTG profile of the pre-carbonized sample also demonstrated that the highest vitality degradation rate arises at about 324°C, suggesting a broad peak. This indicates the simultaneous evaporation process of complex compounds including cellulose, hemicellulose and lignin [39,40]. As a consequence of the weight decrease, about 16% of the final mass was pre-carbonized CFB. Previously reported, cellulose acetate filters created 10 to 15% CFB carbon using the carbonization process and at temperatures ranging from 280 to 360°C, with equivalent results [41].

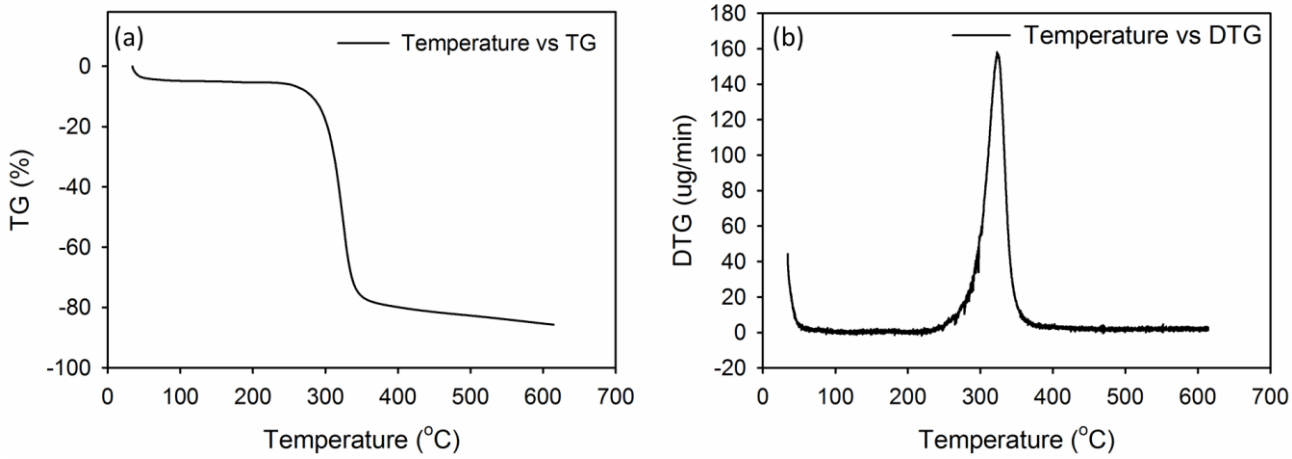

Fig. 1. The pre-carbonized CFB curve of the TG at temperature from 30 °C to 600 °C in (a) and (b) DTG

The slight weight loss was related to volatile decomposition. Other investigations, such as those on date palms, have shown cellulose degradation within the same temperature range [42]. Table 1 shows the density (ρ) and elemental analysis of the ACFC samples before and after carbonization. Sample ACFC-2 had the greatest density, measuring 1.09 g cm^{-3}, whereas sample ACFC-1 had the lowest density, measuring 1.01 g cm^{-3}. Whenever the mass ratio of the KOH activator is increased, the particles get smaller and the number of holes for the production of micropores increases. The quantity of high surface area created in the electrode material is determined by the number of porous densities in the sample [43]. The density of the sample ACFC-2 increases as the carbon element increases.

Meanwhile, sample ACFC-1 had the greatest value due to the conditions before the carbonization procedure, whereas sample ACFC-2 had the lowest value. This state is related to the activating agent percentage, indicating that more pores were formed in the pre-carbonized CFB samples. As shown in Table 1, all samples contain C and O atoms. Sample ACFC-1 has a C and O content of 93.33; 6.67 (wt.%) and sample ACFC-2 has a C and O content of 94.56; 5.44 (wt.%), which is barely higher than the activated carbon from different biomass precursor [25,41].

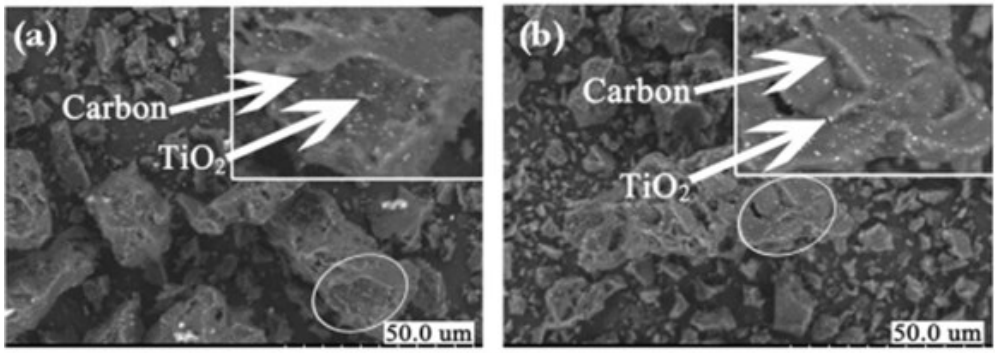

Fig. 2. (a) and (b) SEM image of ACFC-1 and ACFC-2 samples

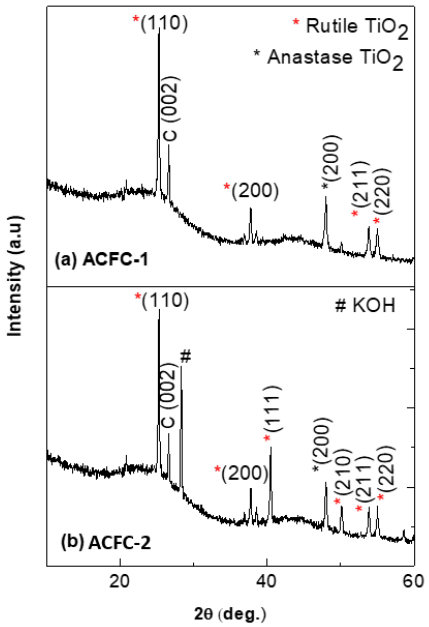

Fig. 3. XRD pattern of (a) ACFC-1 and (b) ACFC-2 samples

Table 1. density and elemental composition

Sample	Before carbonization (g cm^{-3})	After carbonization (g cm^{-3})	Element (wt.%) C	O
ACFC-1	1.29	1.01	93.33	6.67
ACFC-2	1.18	1.09	94.56	5.44

Fig. 2(a) and Fig. 2(b) show SEM images (x1000) of ACFC-1 and ACFC-2 samples generated from CFB. The pre-carbonized CF ball milling procedure is responsible for the irregular form and rough surface structure. Fig. 2(b) depicts the ACFC-1's large clusters and bulky surfaces, which have a diameter of more than 10 microns and a length of more than 50 microns, as well as those small TiO_2 nanoparticles. TiO_2 white spot-like particles were evenly dispersed on the surface (indicated by white arrows). According to Barakat et al. (2023), the production of nano-structured TiO_2-AC composite has particle sizes that range from 10 to 20 nm with a non-uniform distribution [44]. XRD measurements revealed the existence of TiO_2 nanoparticles in that sample. White spot-like particles (labeled by white arrows) were uniformly distributed on the surface.

The presence of amorphous carbon is shown by the XRD patterns of the two samples (ACFC-1 and ACFC-2). As shown in Fig. 3(a), the spectra reveal one peak (002). The broad peak is placed at an angle 2θ of about 21° to 24° reflecting the typical amorphous carbon planes of 002 and 100, respectively [45]. In addition, the others peaks are TiO_2 rutile and anastase structure (JCPDS No. 75-1537). It was discovered in prior research published in the literature [46]. Based on this analysis, an incomplete graphitization at a relatively low temperature of 600°C is recommended. Interestingly, the three reflections (110), (111), and (210) of the TiO_2 rutile structure becomes visible in Fig. 3(b). The appearance of these reflections suggested the presence of TiO_2 nanoparticles. The pattern indexed to be TiO_2 anatase structure with the lattice parameters a=b=0.3792 nm and c=0.9631 nm for ACFC-1 and a=b=0.3792 nm and c=0.9533 nm for ACFC-2, which are roughly similar to the published data TiO_2 lattice parameters: a=b=0.3789 nm and c=0.9537 nm [47]. The average crystalline size of ACFCs at 9.15 nm was calculated using the Scherer formula. This result is relatively lower compared to the TiO_2-AC composite (10-20nm) reported by Barakat et al. (2023) [44].

The average crystalline size agrees with previous spherically AC results, which act as enhanced support for TiO_2 carbon photocatalysts [48]. In fibers and plastic materials, titanium dioxide pigments with particle sizes that range from 0.2 to 0.3 microns are commonly de-lustered with whitening agents [49]. TiO_2 is used as an additive cigarette filter to induce the photo-degradation of the cellulose acetate into the environment [50]. The presence of Ti in the cigarette filter was not detected by EDX analysis, which could be attributed to its low concentration (<1 ppm) [51]. Table 2 shows that as the CFB/KOH ratio increases, the value of d_{002} increases more than the value of d_{100}. At 1000-1350 °C, the d_{002} of ACFCs is greater than the d_{002} of graphite (0.3354 nm) [52]. ACFC carbonization is more complicated than that of other carbon materials due to the high cellulose liquefaction complexity [53]. With an increase in the CFB/KOH ratio, L_c increases while L_a decreases, indicating cigarette filter carbon (CFC) graphitization degree (L_c/d_{002}). Table 2 summarizes the surface area of CFCs obtained from N_2 adsorption isotherms. The surface area of CFCs increases from 239 to 472 m^2 g^{-1} with an increase in the KOH ratio from 2 to 4. This surface area is comparable to previous research on porous carbon

from different sources [54,55].

Table 2. XRD structure and BET surface area parameters of ACFCs

Sample	d_{002} (nm)	d_{100} (nm)	L_c (nm)	L_a (nm)	S_{BET} ($m^2 g^{-1}$)
ACFC-1	0.3569	0.2051	1.30	0.95	239
ACFC-2	0.3568	0.2063	1.84	0.74	472

To study the physisorption of molecules of gas on a surface which is principle to identify the total surface area, theory of Brunauer, Emmett, and Teller (BET) is applied. BET theory was the extension of Langmuir's kinetic theory [33]. However, in BET theory, it is assumed that in the multilayer adsorption system, adsorption energy (E_i) of 2nd layer or more has the identical value of the heat of vaporization (E_L) [35]. Fig. 4 demonstrate $1/(W[P/P_0-1])$ vs. P/P_0 linear plot in the range of $0.05 \leq P/P_0 \leq 0.3$ for ACFC-1 and ACFC-2 samples. The correlation coefficient values of both samples are close to unity. Thus, it shows the best fit of data based on eq. (2) and (3). The calculated parameters are listed in Table 3.

Apparently, the surface area of the ACFC-2 sample (471.764 $m^2 g^{-1}$) is larger than ACFC-1 (239.459 $m^2 g^{-1}$), which proves the enhancement of capacitance from 24 F g^{-1} to 87 F g^{-1}, which is in agreement with a published article [19]. Wang et al. (2022) asserted that activated carbon surface area or porosity may affect the capacitance value [56]. Increasing the KOH ratio in ACFC significantly accelerates the surface area of carbon materials up to 2 times in ACFC-2. The increased KOH ratio allows successive reactions with carbon chains to become more intense, thus forming abundant pores [25,57]. The reaction of KOH and carbon is described in several previous articles [24], where the sequential reactions that occur allow the etching of high carbon chains to provide abundant surface area [58]. This allows carbon materials to store large amounts of ions and increase the capacitance value in supercapacitor devices [59].

According to Hill et al. [38], one layer of gas molecules should completely cover the surface to have an adequate adsorption process. However, there can be empty sites, which are called a fraction of surface (θ0) m, on the surface. Obviously, the value of the fraction of surface depends on C. The boundless value of C is an indication of a strong interaction between adsorbate and adsorbent. Also, C=100 can be considered a magical value to indicate high interaction. As a result, C values close to or much higher than 100 demonstrate adequate adsorption to form a monolayer as well as a high interaction between gas molecules and the surface. However, the BET surface area, in terms of physical meaning, is uncertain for C values that are significantly lower than the magical number of C.

Table 3. The BET parameters of ACFC-1 and ACFC-2 samples

Sample	W_m	C	S	Correlation coefficient, r	$(\theta_0)_m$
ACFC-1	0.069	20.71	239.459	0.997	0.18
ACFC-2	0.135	81.88	471.764	0.998	0.01

According to Table 3, the value of C for the ACFC-1 sample is much less than 100, while the value for the ACFC-2 sample is almost close to 100, which demonstrates a good interaction between molecules of N_2 gas and the ACFC-2 surface. Thus, its unoccupied sites are less (θ0, ACCF-2<θ0, ACCF-1).

As it was asserted, sufficient adsorption occurs when one layer of molecules occupies the surface, but there are still some unoccupied sites that can be defined as a fraction of the surface. Now, for evaluation of fractional surface coverage of molecule layers at different depths. Table 4 indicates the fractional surface for different values of i for the ACFC-1 and ACFC-2 samples. As a result, the fraction of the surface covered by gas molecules is demonstrated without regard for their arrangement or mobility.

Table 4. $(\theta_i)_m$ values of ACFC-1 and ACFC-2 samples for various i

i	$(\theta_i)_m$	
	ACFC-1 (C=20.71)	ACFC-2 (C=81.88)
i=1	0.6710	0.00819
i=2	0.1208	0.00008
i=3	0.0217	
i=4	0.0039	
i=5	0.0007	
i=6	0.0001	

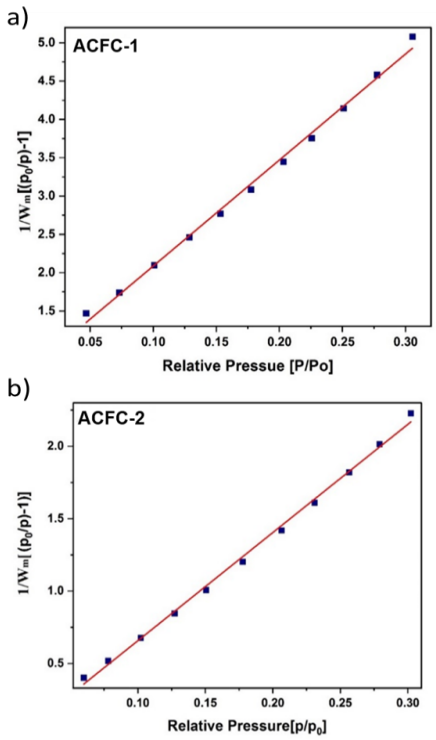

Fig. 4. $1/(W[P/P_0-1])$ vs. P/P_0 curve for ACFC-1 and ACFC-2 sample

The nitrogen adsorption isotherms of ACFC-1 and ACFC-2 samples are shown in Fig. 5 Regarding the six isotherm types categorized by IUPAC [60], both plots belong to the first type of adsorption isotherm that is reversible. The shape of the plot is concave, and the number of adsorbed substances is specified in the relative pressure. The N_2 adsorption-desorption curve provides qualitative information on the carbonaceous material's adsorption mechanism and porous structure. Generally, this kind of behavior has been observed

in the physical adsorption of micro-porous materials. Filling of micro-porous materials and, finally, the high adsorption, can be observed at relatively low pressures [61]. In this type of isotherm, only several layers of adsorption can occur. To sum up, the first type of adsorption isotherm has a great slope due to the high intensity of adsorption [62]. Finally, they can be formed like a horizontal line, which determines the stabilization of the adsorption process in which the sites and pores are saturated with molecules and there are no unoccupied sites [32,63].

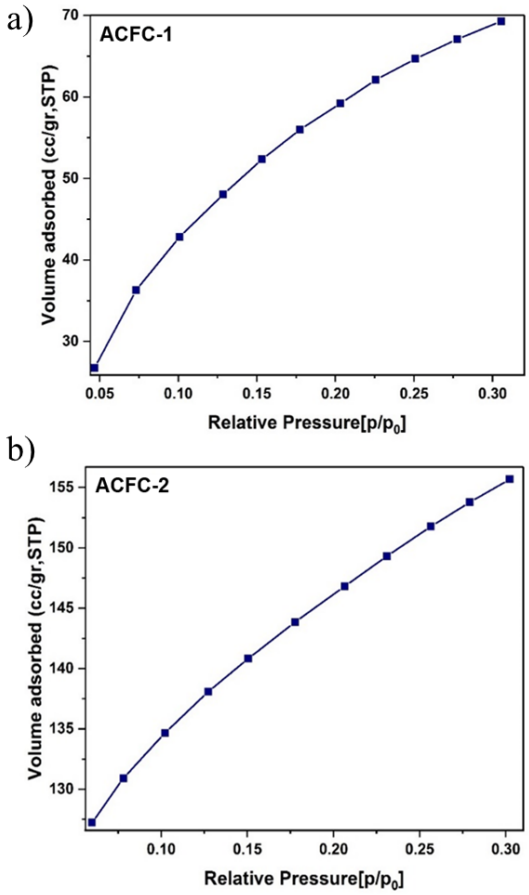

Fig. 5. Adsorption isotherm curve for ACFC-1 and ACFC-2 samples

As shown in Fig. 5, the volume adsorbed increases as the relative pressure (P/P_0) increases. According to ACFC-1, the maximum value of volume adsorbed equals 69.28 cc gr^{-1} when relative pressure is 0.3. The volume adsorbed by the ACFC-2 sample, on the other hand, has nearly reached 155.68 cc gr^{-1}. Table 2 summarizes the surface area of ACFCs derived from N_2 adsorption isotherms. The data show that increasing the KOH ratio from 2 to 4 increases the BET surface area of ACFCs from 239 to 472 $m^2\ g^{-1}$.

To confirm the electrochemical characterization of the as-prepared electrode in aqueous 1.0 M H_2SO_4 electrolytes at room temperature, the current-potential curve of the electrode ACFCs from CV measurements is depicted in Fig. 6. The curve's nearly quasi-rectangular shape reflects the charge-discharge capacitive performance of the ACFCs. The charge-discharge curve is used to calculate the specific capacitance (Cs) using the equation $Cs = (I_c\text{-}I_d)m^{-1}.s^{-1}$ (where I is in amperes, m is in grams, and s is the scan rate in millivolts per second) [64]. These represent the applied current, the discharge time, the mass of the electrode material, and the voltage range, respectively. The specific capacitance of (ACFC-1) cell ~24.48 F g^{-1} and (ACFC-2) cell ~87.17 F g^{-1} was obtained with a potential window 0 to 0.5 V at a scan rate of 1 mV s^{-1}. A CFB/KOH activation ratio of 1:4 (ACFC-2) produced the highest specific capacitance value. Because of limited ion diffusion in the electrode, ACFC-1 had a low specific capacitance and weak surface area adsorption of carbon [65,66].

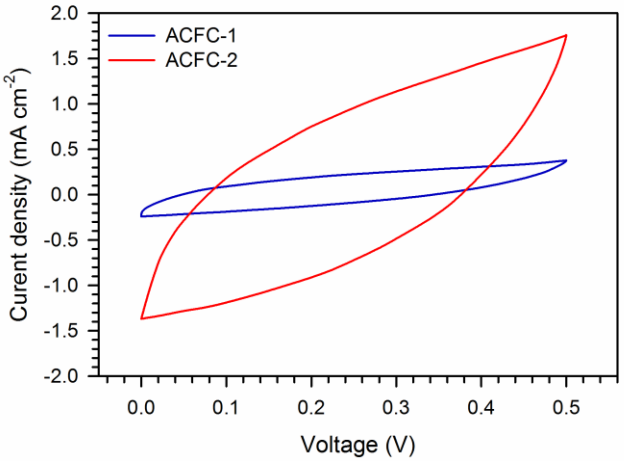

Fig. 6. CV profile of ACFC-1 and ACFC-2

This research revealed that the dependence of capacitive performance on KOH activation ratio facilitates ion adsorption and speeds ion transport in the surface area of carbon, influencing the charge-discharge characteristics of the electrode materials. As a result, the increased surface area reduces internal resistance and increases the production of carbon structures, which improves electrochemical performance. Table 5 summarizes some reports that used the original material derived from cellulose fibers.

Table 5. Comparison of the specific capacitance of carbon materials derived from different sources

Sample sources	C_s (F g^{-1})	Ref.
European hornbeam	24	[54]
Banana stem	74	[67]
MnO_2 nanofiber	37	[68]
Terminalia Catappa leaf	54	[39]
Cigarette filters	52	[19]
Cigarette filter butts	87	This work

This variation in capacitive value can be attributed to a number of factors, including the activating agent, the method of testing the electrochemical properties, the electrolytes, and the origin of the cellulose material produced in each AC's different pores. In addition, this cigarette butt recycling process can be utilized for supercapacitor applications and absorbing other metal nitrides, such as Fe^{3+}, Co^{2+}, and Ni^{2+} ions.

According to the current research results, cigarette filter

waste comprises recycled activated cigarette filter carbons and their characteristics. The samples' XRD patterns revealed two peaks in carbon with crystal orientation (002) and a strong reflection peak (110) with a maximum intensity of TiO_2 nanoparticles and an average crystal size of 9.15 nm, respectively. The structural parameters (d_{002}) changed significantly in ACFCs with low surface areas, but the L_c increased from 1.3 to 1.84 nm as the surface area increased. The BET surface area of ACFCs rises from 239 to 472 m^2 g^{-1} when the KOH ratio increases from 2 to 4. The capacitance performance of activated ACFCs was improved by increasing the surface area and mass ratio CFB:KOH (1:4); the electrochemical properties electrode has an optimal specific capacitance of 87.1 F g^{-1}. Preliminary research suggests that ACFC generated from CFBs might be used as a supercapacitor electrode.

4. Conclusion

According to the current research results, cigarette filter waste comprises recycled activated cigarette filter carbons and their characteristics. The samples' XRD patterns revealed two peaks in carbon with crystal orientation (002) and a strong reflection peak (110) with a maximum intensity of TiO_2 nanoparticles and an average crystal size of 9.15 nm, respectively. The structural parameters (d_{002}) changed significantly in ACFCs with low surface areas, but the Lc increased from 1.3 to 1.84 nm as the surface area increased. The BET surface area of ACFCs rises from 239 to 472 m^2g^{-1} when the KOH ratio increases from 2 to 4. The capacitance performance of activated ACFCs was improved by increasing the surface area and mass ratio CFB:KOH (1:4); the electrochemical properties electrode has an optimal specific capacitance of 87.1 F g^{-1}. Preliminary research suggests that ACFC generated from CFBs might be used as a supercapacitor electrode.

Acknowledgements

The author would like to thank for Department of Physics, University of Riau, Pekanbaru, Indonesia.

References

1. S. Rawat, R.K. Mishra, T. Bhaskar, Biomass derived functional carbon materials for supercapacitor applications, Chemosphere. 286 (2022) 131961.
2. R.T. Ayinla, J.O. Dennis, H.M. Zaid, Y.K. Sanusi, F. Usman, L.L. Adebayo, A review of technical advances of recent palm bio-waste conversion to activated carbon for energy storage, J. Clean. Prod. 229 (2019) 1427–1442.
3. X. Li, J. Zhang, B. Liu, Z. Su, A critical review on the application and recent developments of post-modified biochar in supercapacitors, J. Clean. Prod. 310 (2021) 127428..
4. J. Puls, S.A. Wilson, D. Hölter, Degradation of Cellulose Acetate-Based Materials: A Review, J. Polym. Environ. 19 (2011) 152–165.
5. C. Yan, S. Jia, J. Wei, J. Guan, Z. Shao, Efficient dual conductive network based on layered double hydroxide nanospheres and nanosheets anchored in N-carbon nanofibers for asymmetric supercapacitors, J. Alloys Compd. 930 (2023) 167332.
6. S. Gupta, S.C. Howard, S.P. Hunger, F.G. Antillon, M.L. Metzger, T. Israels, M. Harif, C. Rodriguez-Galindo, Treating Childhood Cancer in Low- and Middle-Income Countries, Dis. Control Priorities, Third Ed. (Volume 3) Cancer. (2015) 121–146.
7. Y. Liu, R. Qu, X. Li, Y. Wei, L. Feng, Discarded cigarette butts regenerated hydrophobic-oleophilic materials for both immiscible and emulsified oil/water separation through a wettability reversal strategy, Appl. Surf. Sci. 532 (2020) 147350.
8. J. Zhang, H. Xu, J. Guo, T. Chen, H. Liu, Superhydrophobic polypyrrole-coated cigarette filters for effective oil/water separation, Appl. Sci. 10 (2020).
9. R. Li, X. Tian, M. Wei, A. Dong, X. Pan, Y. He, X. Song, H. Li, Flexible pressure sensor based on cigarette filter and highly conductive MXene sheets, Compos. Commun. 27 (2021) 100889.
10. M.T. Rahman, A. Mohajerani, F. Giustozzi, Possible recycling of cigarette butts as fiber modifier in bitumen for asphalt concrete, Materials (Basel). 13 (2020) 1–20.
11. R. Bandi, N.P. Devulapalli, R. Dadigala, B.R. Gangapuram, V. Guttena, Facile Conversion of Toxic Cigarette Butts to N,S-Codoped Carbon Dots and Their Application in Fluorescent Film, Security Ink, Bioimaging, Sensing and Logic Gate Operation, ACS Omega. 3 (2018) 13454–13466.
12. G. Shah, U. Bhatt, V. Soni, A comprehensive review on triple R eco-management strategies to reduce, reuse and recycle of hazardous cigarette butts, Heliyon. 9 (2023) e16642.
13. M.B. d'Heni Teixeira, M.A.B. Duarte, L. Raposo Garcez, J. Camargo Rubim, T. Hofmann Gatti, P.A.Z. Suarez, Process development for cigarette butts recycling into cellulose pulp, Waste Manag. 60 (2017) 140–150.
14. A. Sabzali, M. Nikaeen, B. Bina, Application of cigarette filter rods as biofilm carrier in an integrated fixed-film activated sludge reactor, Water Sci. Technol. 67 (2013) 1793–1801.
15. Y. Yue, Y. Liu, W. Zhang, J. Guo, Y. Gong, Y. Yu, Amidoxime functionalized low-cost cellulose-based adsorbent derived from waste cigarette filters for efficient heavy metal removal, J. Environ. Chem. Eng. 10 (2022). .
16. T. Wang, F. Yin, Y. Fang, C. Sun, Waste Cigarette Butts-Derived Nitrogen-Doped Carbon Fibers Loaded with Ru Nanoparticles as an Efficient Cathode Catalyst for Lithium-Oxygen Batteries, ACS Sustain. Chem. Eng. 11 (2023) 9163–9171.
17. C. Yu, H. Hou, X. Liu, L. Han, Y. Yao, Z. Dai, D. Li, The recovery of the waste cigarette butts for N-doped carbon anode in lithium ion battery, Front. Mater. 5 (2018) 1–9.
18. Y.F. Wu, Y.C. Hsiao, Y.J. Ou, S. Kubendhiran, C.Y. Huang, S. Yougbaré, L.Y. Lin, Synthesis of cigarette filter-derived activated carbon using various activating agents for flexible capacitive supercapacitors, J. Energy Storage. 54 (2022).
19. R. Bi, S.K. Pang, K.C. Yung, L.K. Yin, Comprehensive study of used cigarette filters-derived porous activated carbon for Supercapacitors: From biomass waste to sustainable energy source, J. Electroanal. Chem. 925 (2022).
20. A.M. Abioye, F.N. Ani, Recent development in the production of activated carbon electrodes from agricultural waste biomass for supercapacitors: A review, Renew. Sustain. Energy Rev. 52 (2015) 1282–1293..
21. Q. Xiong, Q. Bai, C. Li, H. Lei, C. Liu, Y. Shen, H. Uyama, Cost-effective, highly selective and environmentally friendly superhydrophobic absorbent from cigarette filters for oil spillage clean up, Polym. 10 (2018) 1101.

22. A.R. Selvaraj, A. Muthusamy, In-ho-Cho, H.J. Kim, K. Senthil, K. Prabakar, Ultrahigh surface area biomass derived 3D hierarchical porous carbon nanosheet electrodes for high energy density supercapacitors, Carbon N. Y. 174 (2021) 463–474.
23. B. Shaku, T.P. Mofokeng, N.J. Coville, K.I. Ozoemena, Biomass valorisation of marula nutshell waste into nitrogen-doped activated carbon for use in high performance supercapacitors, Electrochim. Acta. 442 (2023) 141828.
24. E. Taer, F. Febriyanti, W.S. Mustika, R. Taslim, A. Agustino, A. Apriwandi, Enhancing the performance of supercapacitor electrode from chemical activation of carbon nanofibers derived Areca catechu husk via one-stage integrated pyrolysis, Carbon Lett. (2020).
25. E. Taer, L. Pratiwi, Apriwandi, W.S. Mustika, R. Taslim, Agustino, Three-dimensional pore structure of activated carbon monolithic derived from hierarchically bamboo stem for supercapacitor application, Commun. Sci. Technol. 5 (2020) 22–30.
26. S. Saini, P. Chand, A. Joshi, Biomass derived carbon for supercapacitor applications: Review, J. Energy Storage. 39 (2021) 102646.
27. S. Majid, A.S.G. Ali, W.Q. Cao, R. Reza, Q. Ge, Biomass-derived porous carbons as supercapacitor electrodes-A review, New Carbon Mater. 36 (2021) 546–572.
28. E. Taer, Apriwandi, Windasari, R. Taslim, M. Deraman, Novel laurel aromatic evergreen biomass derived hierarchical porous carbon nanosheet as sustainable electrode for high performance symmetric supercapacitor, J. Energy Storage. 67 (2023) 107567.
29. X. Xu, L. Yang, K. Zhuo, Z. Zhang, Q. Du, C. Wang, Y. Chen, Y. Zhao, Honeysuckle flowers-derived hierarchical porous carbon matching with ionic liquid electrolyte for high-energy supercapacitors, J. Energy Storage. 41 (2021) 102988.
30. J. Serafin, M. Baca, M. Biegun, E. Mijowska, R.J. Kaleńczuk, J. Sreńscek-Nazzal, B. Michalkiewicz, Direct conversion of biomass to nanoporous activated biocarbons for high CO2 adsorption and supercapacitor applications, Appl. Surf. Sci. 497 (2019) 143722.
31. S. Huo, M. Liu, L. Wu, M. Liu, M. Xu, W. Ni, Y.M. Yan, Synthesis of ultrathin and hierarchically porous carbon nanosheets based on interlayer-confined inorganic/organic coordination for high performance supercapacitors, J. Power Sources. 414 (2019) 383–392.
32. S. Liu, A. Li, Q. Han, C. Yang, H. Li, H. Xia, F. Ouyang, J. Zhou, X. Liu, Oxygen-directed porous activation of carbon nanospheres for enhanced capacitive energy storage, J. Power Sources. 483 (2021) 229223.
33. K.S.W. Sing, Reporting physisorption data for gas/solid systems with special reference to the determination of surface area and porosity, Pure Appl. Chem. 54 (1982) 2201–2218.
34. F. Rouquerol, J. Ruoquerol, K. Sing, Adsorption by powders and porous solids: principles, methodology and applications, in: Adsorpt. by Powders Porous Solids, 1999: pp. 1–26.
35. R. Bardestani, G.S. Patience, S. Kaliaguine, Experimental methods in chemical engineering: specific surface area and pore size distribution measurements—BET, BJH, and DFT, Can. J. Chem. Eng. 97 (2019) 2781–2791.
36. E. Taer, M. Deraman, R. Taslim, Iwantono, Preparation of binderless activated carbon monolith from pre-carbonization rubber wood sawdust by controlling of carbonization and activation condition, AIP Conf. Proc. 1554 (2013) 33–37.
37. E. Taer, Iwantono, S.T. Manik, R. Taslim, D. Dahlan, M. Deraman, Preparation of activated carbon monolith electrodes from sugarcane bagasse by physical and physical-chemical activation process for supercapacitor application, Adv. Mater. Res. 896 (2014) 179–182.
38. E. Taer, N. Yanti, W.S. Mustika, A. Apriwandi, R. Taslim, A. Agustino, Porous activated carbon monolith with nanosheet/nanofiber structure derived from the green stem of cassava for supercapacitor application, Int. J. Energy Res. 44 (2020) 1–14.
39. E. Taer, A. Afrianda, R. Taslim, Krisman, Minarni, A. Agustino, A. Apriwandi, U. Malik, The physical and electrochemical properties of activated carbon electrode made from Terminalia Catappa leaf (TCL) for supercapacitor cell application, J. Phys. Conf. Ser. 1120 (2018) 012007.
40. R. Farma, M. Deraman, R. Omar, Awitdrus, M.M. Ishak, E. Taer, I.A. Talib, Binderless composite electrode monolith from carbon nanotube and biomass carbon activated by KOH and CO2 gas for supercapacitor, AIP Conf. Proc. 1415 (2011) 180–184.
41. A. Sarwar, M. Ali, A.H. Khoja, A. Nawar, A. Waqas, R. Liaquat, S.R. Naqvi, M. Asjid, Synthesis and characterization of biomass-derived surface-modified activated carbon for enhanced CO2 adsorption, J. CO2 Util. 46 (2021) 101476.
42. E. Taer, A. Apriwandi, A. Agutino, R. Taslim, W.S. Mustika, Exa Fadli, Surface modification: unique ellipsoidal/strobili-fiber structure of porous carbon monolith for electrode supercapacitor, Nanosci. Technol. An Int. J. 12 (2021) 45–63.
43. E. Taer, F. Hasanah, R. Taslim, Nanofiber-enrich activated carbon coin derived from tofu dregs as electrode materials for supercapacitor, Commun. Sci. Technol. 6 (2021) 41–48.
44. N.A.M. Barakat, Y.T. Sayed, O.M. Irfan, M.M. Abdelaty, Synthesis of TiO2-incorporated activated carbon as an effective Ion electrosorption material, PLoS One. 18 (2023) 1–11.
45. E. Taer, N. Yanti, R. Taslim, A. Apriwandi, Interconnected micro-mesoporous carbon nanofiber derived from lemongrass for high symmetric supercapacitor performance, J. Mater. Res. Technol. 19 (2022) 4721–4732.
46. F. Scarpelli, T.F. Mastropietro, T. Poerio, N. Godbert, Mesoporous TiO2 Thin Films: State of the Art, in: Titan. Dioxide - Mater. a Sustain. Environ., 2018: pp. 57–80.
47. S.A. Hamdan, I.M. Ibrahim, I.M. Ali, Comparison of anatase and rutile TiO2 nanostructure for gas sensing application, Dig. J. Nanomater. Biostructures. 15 (2020) 1001–1008.
48. J. Zhang, M. Vasei, Y. Sang, H. Liu, J.P. Claverie, TiO2@Carbon Photocatalysts: The Effect of Carbon Thickness on Catalysis, ACS Appl. Mater. Interfaces. 8 (2016) 1903–1912.
49. C. Lim, H.R. An, H. Lee, R. Lee, Y. Choi, J.I. Park, J. Yoon, H.U. Lee, Y.S. Lee, Carbon-titanium dioxide heterogeneous (photo)catalysts (C–TiO2) for highly efficient visible light photocatalytic application, Compos. Part B Eng. 241 (2022) 109997.
50. F.X. Joly, M. Coulis, Comparison of cellulose vs. plastic cigarette filter decomposition under distinct disposal environments, Waste Manag. 72 (2018) 349–353.
51. N.H. Mohd, H. Kargazadeh, M. Miyamoto, S. Uemiya, N. Sharer, A. Baharum, T. Lee Peng, I. Ahmad, M.A. Yarmo, R. Othaman, Aminosilanes grafted nanocrystalline cellulose from oil palm empty fruit bunch aerogel for carbon dioxide capture, J. Mater. Res. Technol. 13 (2021) 2287–2296.
52. E. Taer, A. Apriwandi, S. Chow, R. Taslim, Integrated pyrolysis approach of self-O-doped hierarchical porous carbon from yellow mangosteen fruit for excellent solid-state supercapacitor volumetric performance, Diam. Relat. Mater. 135 (2023) 109866.
53. S. Saha, D. Potphode, C.S. Sharma, Borassus flabellifer Fruit Flesh Derived Hierarchical Porous Partly Graphitic Carbon as a Sustainable Electrode for Supercapacitors, Energy and Fuels. 36 (2022) 638–654.
54. A. Jain, M. Ghosh, M. Krajewski, S. Kurungot, M. Michalska, Biomass-derived activated carbon material from native European deciduous trees as an inexpensive and sustainable energy material for supercapacitor

application, J. Energy Storage. 34 (2021) 102178.
55. R. Taslim, A. Apriwandi, E. Taer, Novel Moringa oleifera Leaves 3D Porous Carbon-Based Electrode Material as a High-Performance EDLC Supercapacitor, ACS Omega. 7 (2022) 36489–36502.
56. J. Wang, Y. Xu, M. Yan, B. Ren, X. Dong, J. Miao, L. Zhang, X. Zhao, Z. Liu, Preparation and application of biomass-based porous carbon with S, N, Zn, and Fe heteroatoms loading for use in supercapacitors, Biomass and Bioenergy. 156 (2022) 106301.
57. E. Taer, A. Apriwandi, N. Nursyafni, R. Taslim, Averrhoa bilimbi leaves-derived oxygen doped 3D-linked hierarchical porous carbon as high-quality electrode material for symmetric supercapacitor, J. Energy Storage. 52 (2022) 104911.
58. S.X. Liang, F.F. Duan, Q.F. Lü, H. Yang, Hierarchical Biocarbons with Controlled Micropores and Mesopores Derived from Kapok Fruit Peels for High-Performance Supercapacitor Electrodes, ACS Omega. 4 (2019) 5991–5999.
59. Y. Fu, N. Zhang, Y. Shen, X. Ge, M. Chen, Micro-mesoporous carbons from original and pelletized rice husk via one- step catalytic pyrolysis, Bioresour. Technol. 269 (2018) 67–73.
60. C. Ding, T. Liu, X. Yan, L. Huang, S. Ryu, J. Lan, Y. Yu, W.H. Zhong, X. Yang, AN Ultra-microporous carbon material boosting integrated capacitance for cellulose-based supercapacitors, Nano-Micro Lett. 12 (2020) 63.
61. V.S. Bhat, P. Kanagavalli, G. Sriram, R.P. B, N.S. John, M. Veerapandian, M. Kurkuri, G. Hegde, Low cost, catalyst free, high performance supercapacitors based on porous nano carbon derived from agriculture waste, J. Energy Storage. 32 (2020) 101829.
62. Y. Wang, M. Qiao, X. Mamat, Nitrogen-doped macro-meso-micro hierarchical ordered porous carbon derived from ZIF-8 for boosting supercapacitor performance, Appl. Surf. Sci. 540 (2021) 148352.
63. C. Ma, L. Wu, M. Dirican, H. Cheng, J. Li, Y. Song, J. Shi, X. Zhang, ZnO-assisted synthesis of lignin-based ultra-fine microporous carbon nanofibers for supercapacitors, J. Colloid Interface Sci. 586 (2021) 412–422.
64. E. Taer, N. Nursyafni, A. Apriwandi, R. Taslim, Novel Solanum torvum Fruit Biomass-Derived Hierarchical Porous Carbon Nanosphere as Excellent Electrode Material for Enhanced Symmetric Supercapacitor Performance, JOM. (2023).
65. Q. Li, Y. Jiang, Z. Jiang, J. Zhu, X. Gan, F. Qin, T. Tang, W. Luo, N. Guo, Z. Liu, L. Wang, S. Zhang, D. Jia, Z. Fan, Ultrafast pore-tailoring of dense microporous carbon for high volumetric performance supercapacitors in organic electrolyte, Carbon N. Y. 191 (2022) 19–27.
66. X. Wu, Y. Wang, R. Zhong, B. Li, Nitrogen and sulfur dual-doped hierarchical porous carbon derived from bacterial cellulose for high performance supercapacitor, Diam. Relat. Mater. 116 (2021) 108447.
67. V. Subramanian, C. Luo, A.M. Stephan, K.S. Nahm, S. Thomas, B. Wei, Supercapacitors from activated carbon derived from banana fibers, J. Phys. Chem. C. 111 (2007) 7527–7531.
68. K. Xu, S. Li, J. Yang, J. Hu, Hierarchical hollow MnO2 nanofibers with enhanced supercapacitor performance, J. Colloid Interface Sci. 513 (2018) 448–454.